EES Solar

PAPER

View Article Online
View Journal | View Issue

Cite this: *EES Sol.*, 2025, **1**, 193

Spin-coating processing of an oriented Sb_2S_3 layer for PV applications: effect of the precursors and device architecture

Nathan Daem, Marie-Julie Charlier, Gilles Spronck, Pierre Colson, Rudi Cloots* and Jennifer Dewalque

Received 5th December 2024
Accepted 16th February 2025

DOI: 10.1039/d4el00036f

rsc.li/EESSolar

Sb_2S_3 stands out as a low-toxicity, promising material for photovoltaic applications because of its unique optoelectronic properties such as a suitable band gap (1.4–1.8 eV), a high absorption coefficient (10^5 cm^{-1}), appreciable thermal and chemical stability, and a high tolerance to defects. In the first part of this study, $Sb(Ac)_3$ and $SbCl_3$ are compared as antimony precursors for the formation of the Sb_2S_3 photoactive film. The $Sb(Ac)_3$/thiourea (TU) precursor solution allows the formation of films with higher coverage and uniformity compared to films obtained from $SbCl_3$/TU. In terms of PV efficiencies, $Sb(Ac)_3$/TU and $SbCl_3$/TU based layers respectively lead to 4.9% and 4.8% efficiencies. Indeed, the band gap of the Sb_2S_3 layer obtained from $Sb(Ac)_3$/TU (1.75 eV) is less favorable than that from $SbCl_3$/TU (1.65 eV). In addition, the [*hk*1] crystalline orientation of Sb_2S_3 is more favorable for efficient charge transfer in the devices and is more prevalent in the $SbCl_3$/TU films. In the second part, the incorporation of a mesoporous TiO_2 network is considered to improve charge transport at the Sb_2S_3/TiO_2 electron transport layer interface and hence enhance the efficiency of the devices. However, the PV efficiencies are significantly lower in the case of the mesoporous architecture, which is mainly attributed to a [*hk*0] misorientation of the crystals in the mesoporous architecture leading to poor charge transfer. By studying the impact of the antimony precursor and the nature of the TiO_2 electron transport underlayer (dense or mesoporous) on the properties of the Sb_2S_3 photoactive film, we highlight that a combination of three factors is crucial to boost device efficiencies: uniformity/coverage, adequate bandgap, and more importantly crystalline orientation.

Broader context

Antimony sulfide (Sb_2S_3) is a promising material for photovoltaics due to its low toxicity, suitable bandgap (1.4–1.8 eV), high absorption coefficient (~10^5 cm^{-1}), and defect tolerance. This study is among the first to explore how the choice of antimony precursor and electron transport layer architecture influences the performance of Sb_2S_3-based solar cells. Comparing $Sb(Ac)_3$/TU and $SbCl_3$/TU as precursors revealed differences in film coverage, uniformity, and crystalline orientation, with $SbCl_3$ yielding a more favorable bandgap (1.65 eV) and better charge transfer due to its [*hk*1] orientation. Additionally, the incorporation of mesoporous TiO_2 for charge transport was investigated, but this architecture showed lower efficiency due to crystal misorientation ([*hk*0]). These findings highlight the critical role of precursor selection, bandgap alignment, and crystalline orientation in device performance. As a pioneering study, it provides a valuable foundation for further research aimed at optimizing Sb_2S_3 for efficient and sustainable solar energy solutions.

1. Introduction

The development of alternatives to lead-based perovskites is essential to overcome the challenges associated with their stability and toxicity, and to guarantee the long-term success of solar photovoltaic technologies. Chalcogenides have been identified as promising candidates.[1]

A chalcogenide is composed of an element from the chalcogen family (oxygen, sulfur, selenium, tellurium, or polonium) and a group III, IV, VI or transition metal element.[2] Among chalcogenides, scientists are particularly interested in antimony sulfide (Sb_2S_3) because of its excellent optoelectronic properties and low toxicity.

Chalcogenides stand out as promising materials for photovoltaic applications because of their unique optoelectronic properties. In particular, antimony sulfide (Sb_2S_3) has a suitable bandgap (1.4–1.8 eV), a high absorption coefficient (10^5 cm^{-1}), appreciable thermal and chemical stability, and a high tolerance to defects, allowing the manufacture of solar cells that are more robust and less sensitive to process variations.[3]

Stibine Sb_2S_3 has a quasi-one-dimensional (Q1D) crystal structure consisting of $(Sb_4S_6)_n$ ribbons. Each ribbon is made up

Group of Research in Energy and Environment from Materials (GREEnMat), CESAM Research Unit, Chemistry Department, University of Liège, Allée du Six-Août 13, 4000 Liège, Belgium. E-mail: rcloots@uliege.be

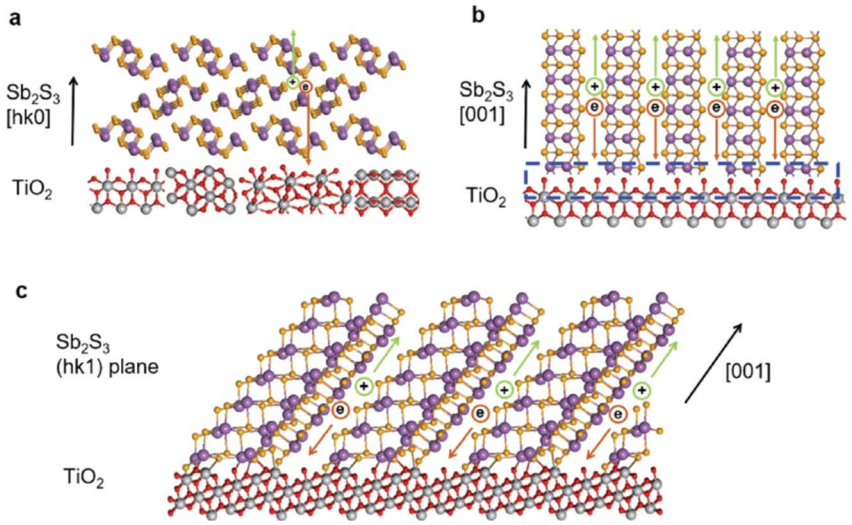

Fig. 1 (a) Crystal structures of $(Sb_4S_6)_n$ ribbons stacked on TiO_2 (a) in the [*hk*0] orientation, (b) in the [001] orientation and (c) in the [*hk*1] orientation. Reproduced with permission from ref. 4. Copyright 2024, John Wiley.

of two triangular-based pyramids of SbS_3 and two square-based pyramids of SbS_5. This anisotropic crystalline structure, unique to Sb_2S_3, induces anisotropic charge transport.[4] The performance of solar cells is therefore linked to the orientation of the ribbons, which are reported to be mainly [*hk*0], [*hk*1] and [001] (Fig. 1).[4] It has been found that charges are transported faster along the [001] orientation. Indeed, charge mobility and conductivity along this orientation are twice as high as those along the [010] orientation and three times as high as those along the perpendicular [100] orientation, as the vertical stacking along the [001] direction favors 1D intra-ribbon transport.[4] In contrast, films with a preferential [*hk*0] orientation, *i.e.* an orientation parallel to the substrate, do not exhibit satisfactory charge transport, as numerous recombination events take place at the interface, due to the inter-ribbon charge hopping mechanism.[5] This orientation is nevertheless the most widespread due to the low surface energy of the Sb_2S_3 ribbons that grow along and spread over the substrate. The above growth process can mainly be attributed to the random crystal facets or low crystallization of the TiO_2 film, which cannot provide reliable epitaxial facets.[6] In addition, the crystal lattice mismatch at the interface between anatase TiO_2 (electron transport layer, ETL) and Sb_2S_3 disfavors a preferential [001] orientation.[7] Furthermore, the large lattice mismatch with TiO_2 can induce interface recombination due to the formation of dangling bonds at Sb_2S_3 ribbon terminals.

In order to reduce recombination and improve charge transport, quasi-epitaxial growth with an [*hk*1] orientation, combining a parallel [*hk*0] and vertical [001] Sb_2S_3/TiO_2 interface is thus a good compromise, guaranteeing efficient intra-ribbon carrier transport and reducing dandling bonds. At the very least, we therefore aim for a [*hk*1] orientation of the stibine coatings in our devices.

The orientation of Sb_2S_3 can also be achieved by optimizing the heat treatment of TiO_2 for lattice-matched tuning.[4] The microtopography of the TiO_2 surface in the anatase phase differs according to the annealing temperature: a smooth and uniform surface with small grains at low temperatures and a highly textured surface with very large, well-defined grains, which facilitates heteroepitaxy, and potentially induces a phase transition to rutile at very high temperatures. Besides, thermal treatment can directly impact oxygen vacancies at the TiO_2 surface.[6] Sb–S clusters with sulfur-rich dangling bonds can bind favorably with titanium atoms at the TiO_2 surface rich in oxygen vacancies. Higher annealing temperatures could introduce more oxygen vacancies, creating sites that may favor subsequent Sb_2S_3 bonding. To match the crystal lattices and bonding sites that facilitate the [*hk*1] orientation of Sb_2S_3, the TiO_2 must be crystallized at a temperature of around 550 °C.[7]

Studies on Sb_2S_3 deposition have been carried out by rapid thermal evaporation,[7] vapor transport deposition and hydrothermal methods.[8,9] In this work, we focused on atmospheric pressure wet-deposition and more specifically spin-coating.

In addition, the literature reports that the orientation of Sb_2S_3 films depends on grain growth theory, influencing the way crystals form.[10] A progressive heat treatment promotes uniform growth with a predominant [*hk*1] orientation. In contrast, rough annealing at high temperatures produces large, flat grains, leading to anomalous growth where the [*hk*0] orientation predominates over [*hk*1]. These results highlight the importance of thermal control in modulating the properties of Sb_2S_3 films. Grains with an [*hk*0] orientation therefore grow faster than grains with an [*hk*1] orientation, leading to abnormal grain growth (Fig. 2).

Most studies use $SbCl_3$/thiourea precursors to form Sb_2S_3 stibine. These studies notably focus on the ratios of $SbCl_3$/TU and S/Sb, precursor concentrations, spin-coating speeds, *etc.* (Table 1). However, efficient Sb_2S_3 solar cells are mostly prepared by chemical bath deposition and hydrothermal methods, which require a large amount of solution and can be time-consuming. These methods achieve PV efficiencies of around 7–8% for the best solar cells (Table 1).

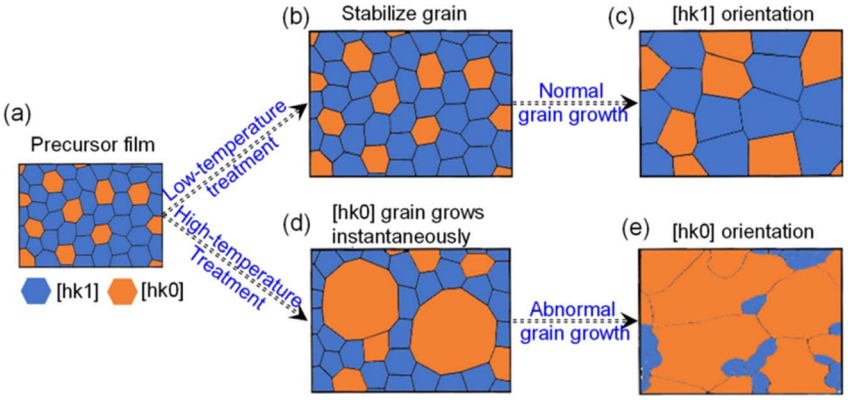

Fig. 2 Mechanism of Sb_2S_3 orientation dependence on grain growth. Surface texture of (a) the Sb_2S_3 precursor film, (b) the Sb_2S_3 precursor film after stabilization at low temperature, and (c) after normal grain growth. (d) and (e) The surface textures of the Sb_2S_3 film after thermal treatment at high temperature and then subjected to abnormal grain growth. Reproduced with permission from ref. 8 Copyright 2024, RSC.

Table 1 Performances of spin-coated Sb_2S_3 devices[11]

	Studied experimental settings	Controlled property	Efficiency (%)	Ref.
$SbCl_3$/thiourea	Spin-coating cycles	Crystallinity	2.3	12
	$SbCl_3$: TU ratio	Grain size	4.4	13
	Annealing temperature	Surface roughness and grain size	4.3	14
	$SbCl_3$: TU ratio	Grain growth and size	2.7	15
	$SbCl_3$ concentration	Uniformity	6.3	16
	Concentration of TU	Surface coverage	5.7	17
	Zn doping	Crystallinity	6.4	18
	Alkali metal doping	Crystallinity and grain size	6.6	19
	Pre-annealing process	Impurity phases	6.8	20
	Doping process	Surface uniformity	1.8	21
	Annealing temperature	Crystallinity	1.7	22
	Spinning speed	Pin holes	2.4	23
	Interfacial layer ($SbCl_3$)	Surface continuity	6.9	24
	Ag doping	Crystallinity	7.7	25
$Sb(Ac)_3$/thiourea	S/Sb ratio	Surface morphology	2.8	24
	Sb_2S_3 seed-mediated growth	Surface defects	5.1	26
	Concentration and S/Sb molar ratio	Film formation	5.7	27

Nevertheless, the devices prepared by spin-coating recently reached a new record power conversion efficiency of 7.7%,[25] which is comparable to the best photovoltaic performances achieved by chemical bath deposition or hydrothermal techniques. This improvement in PV efficiency involved the introduction of silver (Ag) ions into the Sb_2S_3 sol–gel precursors, effectively influencing the crystallization and charge transport characteristics of Sb_2S_3. Consequently, the charge collection efficiency improved, and charge recombination losses decreased. However, in this work, we aim to focus on the pure Sb_2S_3 formulation.

Besides, a few groups use antimony acetate as a source of antimony, with convincing results in terms of PV efficiency.[24,26,27] The best efficiency (5.7%) was obtained by Zhu *et al.* They grew Sb_2S_3 films *in situ* on TiO_2 nanoparticle films and investigated the effects of concentration and the S/Sb molar ratio in the precursor solution on Sb_2S_3 film formation and device performances.[26] Moreover, antimony acetate is generally considered to be less toxic than antimony chloride.

To the best of our knowledge, a comparative study of these two precursors has not been published yet. Comparing the structural and electronic properties of Sb_2S_3 films obtained from both precursors can help in identifying and rationalizing differences in microstructure, crystallinity, grain size, texture, surface morphology and crystal orientations. So, in the first part of this article, we implement $Sb(Ac)_3$/TU and $SbCl_3$/TU precursors for the formation of Sb_2S_3 films and compare their influence on the (micro)structural and optoelectronic properties of the films as well as their impact on the PV performances of the assembled devices.

In addition, in the second part of this work, we compare, for the first time, 2 types of device architectures: "dense" (only dense TiO_2 as ETL) and "mesoporous" (addition of a mesoporous TiO_2 layer between the dense TiO_2 and the photoactive

layer) architectures, to determine the effects of mesoporous TiO_2 in Sb_2S_3 devices.

All in all, this study highlights a combination of three key parameters for improving photovoltaic efficiency in Sb_2S_3 solar cells: uniformity and coverage, an adequate bandgap, and the crystal orientation of the Sb_2S_3 photoactive layer.

2. Experimental section

2.1. Materials and chemicals

Fluorine-doped tin oxide (FTO) coated glass with 2.2 mm thickness and 15 Ω sq^{-1} sheet resistance (TEC15, Greatcell Solar Materials) was used as the substrate. The following chemicals were purchased from various commercial suppliers: hydrochloric acid HCl (VWR, 37%), metallic zinc powder (Roth, ≥98%), titanium diisopropoxide bis(acetylacetonate) TAA (Sigma-Aldrich, 75 wt% in isopropanol), anhydrous ethanol EtOH (Acros, 99.5%), TiO_2 nanoparticle paste 18NR-T (Greatcell Solar Materials), titanium chloride $TiCl_4$ (Merck, ≥97.0%), antimony trichloride $SbCl_3$ (Sigma-Aldrich, >99%), thiourea TU (Sigma-Aldrich, >99%), antimony triacetate $Sb(Ac)_3$ (Sigma-Aldrich, >99.9%), *N*,*N*′-dimethylformamide DMF (Acros Organics, 99.9%), anhydrous chlorobenzene CB (Sigma-Aldrich, 99.8%), 2,2′,7,7′-tetrakis[*N*,*N*-di(4-methoxyphenyl)amino]-9,9′-spirobifluorene – spiro-OMeTAD (Borun, >99.9%), lithium bis(trifluoromethanesulfonyl)imide Li-TFSI (Sigma-Aldrich, 99.95%), 4-*tert*-butylpyridine *t*BP (Sigma-Aldrich, 96%), and anhydrous *n*-butanol *n*-BuOH (Fisher, >99.8%).

2.2. Substrate preparation

First, FTO glass substrates were cut into 2.0 × 2.0 cm^2 pieces and then etched with HCl (2 M) and metallic zinc powder to remove parts of the FTO and prevent short circuits in the final PV cell. Substrates were cleaned in three consecutive washing steps (with soap, ethanol and acetone, respectively) under ultrasonication before being dried under air. A dense hole blocking layer of TiO_2 (c-TiO_2 ~30 nm thick) was then deposited by ultrasonic spray pyrolysis of TAA (2.2 mL) in ethanol (30.0 mL) using a Sono-Tek Exactacoat system combined with an Accumist nozzle. The following spraying parameters were used: a stall power of 3.5 W, an oxygen carrier gas flow of 0.9 psi, a flow rate of 0.25 mL min^{-1}, a nozzle speed of 100 mm s^{-1}, an area spacing of 4 mm, a nozzle-to-substrate distance of 5.5 cm, and a substrate temperature of 450 °C. The deposition pattern was repeated 3 times to obtain a 30 nm thick TiO_2 film. Finally, a post-thermal treatment at 500 °C (ramp 100 °C h^{-1}) was performed for 30 min to crystallize TiO_2 in the anatase phase. After a cleaning treatment under UV-ozone for 15 min, a 150 nm thick mesoporous (mp-)TiO_2 layer was deposited onto the c-TiO_2 layer. Commercial TiO_2 nanoparticle paste (18NR-T, Greatcell Solar Materials) was diluted in absolute ethanol (1 : 9.8 weight ratio) and spin-coated at 1500 rpm for 30 s, followed by subsequent annealing at 500 °C (with a ramp of 100 °C h^{-1}) for 30 min. The mp-TiO_2 layer was immersed in an aqueous $TiCl_4$ solution (4 × 10^{-2} M) for 30 min at 60 °C to further improve the connectivity between the TiO_2 nanoparticles. Then, the samples were successively rinsed with water and EtOH, dried with compressed air and then calcined for 30 min at 450 °C in a preheated oven. Before Sb_2S_3 film deposition, a final cleaning treatment under UV-ozone for 15 minutes was applied to the samples.

2.3. Photoactive Sb_2S_3 film preparation

2.3.1. $Sb(Ac)_3$/TU precursors. A 1 M solution of Sb_2S_3 precursors was prepared outside the glovebox from $Sb(Ac)_3$ and thiourea in a molar ratio of 1 : 1.8. 0.29889 g of $Sb(Ac)_3$ was dissolved in 1 mL of DMF. Once the $Sb(Ac)_3$ was completely dissolved, thiourea was added (m = 0.13702 g) and the mixture was stirred vigorously until the thiourea was completely dissolved. Note that the solution tends to precipitate after one hour.

2.3.2. $SbCl_3$/TU precursors. A 1 M solution of Sb_2S_3 precursors was prepared in a glovebox from $SbCl_3$ and thiourea in the same molar ratio as above (1 : 1.8). 0.22812 g of $SbCl_3$ was dissolved in 1 mL of DMF. Next, 0.13702 g of thiourea was added and the mixture was stirred vigorously for at least 40 min to allow complexation of the two compounds.

2.4. Photoactive Sb_2S_3 film deposition

The $Sb(Ac)_3$/TU and $SbCl_3$/TU solutions were deposited onto the FTO glass/c-TiO_2 substrates by spin-coating at 4200 rpm for 40 s in a glovebox. As mentioned in the Introduction, a temperature gradient is necessary to promote the [*hk*1] orientation of Sb_2S_3 crystals. A heat treatment in several stages was therefore applied: 100 °C (60 min)–180 °C (10 min)–265 °C (30 min), enabling the optimum to be obtained in terms of film morphology (high coverage, uniformity, and smoothness). In addition, in order to further improve the film morphology features, a 1 M TU-DMSO post-treatment was carried out immediately after the last thermal step at 265 °C (30 min). 0.07612 g of TU was added in 1 mL of DMSO. The post-treatment solution was also applied by spin-coating at 5000 rpm for 30 s, followed by a heat treatment at 300 °C for 5 min.

The $SbCl_3$/TU solution was deposited onto the FTO glass/c-TiO_2/mp-TiO_2 substrates by spin-coating at 4200 rpm for 40 s in a glovebox. A multi-step thermal treatment was then applied: 150 °C (10 min)–265 °C (30 min)–300 °C (10 min). No TU-DMSO post-treatment was applied, as this did not improve film properties.

2.5. Solar cell fabrication

First, spiro-OMeTAD (186 mg) and an additive solution (84 μL) were mixed with anhydrous chlorobenzene (2 mL). The additive solution was prepared from 0.175 g of Li-TFSI and 312.5 μL of *tert*-butylpyridine in 1 mL of anhydrous butanol. The solution was then deposited by spin coating at 2000 rpm for 60 s.

After scratching off the TiO_2/Sb_2S_3/spiro-OMeTAD layers from the photoanode contact, a gold counter-electrode layer was deposited by thermal evaporation (using a home-made apparatus) using a patterned mask.

2.6. Characterization

A field emission gun microscope TESCAN CLARA (FEI) operating at a 15 kV accelerating voltage and under high vacuum was used for the morphological characterization of individual layers and assembled cells by scanning electron microscopy (SEM). All samples were coated with gold before characterization.

Optical profilometer images were recorded with an instrument Wyko NT9100 (×20, ×50 objectives) with the measuring mode VSI-VXI, back scan = 10 μm, length = 10 μm.

X-ray diffraction (XRD) was conducted in fixed θ–2θ geometry on a Bruker D8 grazing incidence diffractometer instrument using a Cu Kα source (λ = 1.5406 Å) at a current of 40 A and a voltage of 40 V. All references were taken from the PDF4+ database from the International Center for Diffraction Data.

A Shimadzu 3600 Plus instrument with an integrating sphere (ISR-1503) was used for optical measurements by UV-VIS-NIR spectrometry.

The depth profile of the films was investigated using a Thermo Fisher K-alpha X-ray photoelectron spectrometer (XPS), equipped with a monochromatic Al Kα source and calibrated with the adventitious carbon (C 1s) peak. An Ar ion gun was used to progressively strip (0.3 nm s^{-1}) and then probe the elements as they were removed.

A class A solar simulator (Newport Spectra Physics) coupled to a Keithley 2400 sourcemeter was used to measure the PV conversion efficiency of the cells. Calibration was performed using a KG5 filtered silicon reference solar cell from Newport. Photocurrent density *versus* applied voltage curves (*J*–*V* curves) were measured on 2.0 × 2.0 cm^2 devices under simulated 1 sun illumination (filter AM 1.5) at room temperature, using a black mask with a 0.0355 cm^2 aperture. Forward (0 V to 1.2 V) and backward (1.2 V to 0 V) measurements were performed with an increase of 4 mV (0.2 s per step).

For electrochemical impedance spectroscopy (EIS), data were collected using a BioLogic SP-200 potentiostat (Science Instrument) and analyzed with EC-Lab software. A sinusoidal potential perturbation was applied to the assembled devices and the current variation response was recorded. A frequency range of 3 MHz to 85 mHz with 10 mV sinusoidal modulation was applied for EIS data acquisition. Measurements were performed at room temperature under standard 1 sun illumination (AM 1.5 filter) and under open circuit potential (OCP) conditions.

3. Results and discussion

3.1. Choice of the antimony precursor for the formation of Sb_2S_3

3.1.1. Structure and morphology of Sb_2S_3 thin films. First, the morphology of the Sb_2S_3 films was evaluated by scanning electron microscopy (SEM) analysis (Fig. 3a–d). The $Sb(Ac)_3$/TU precursor solution allows the formation of a very smooth and uniform chalcogenide film whereas $SbCl_3$/TU-based films

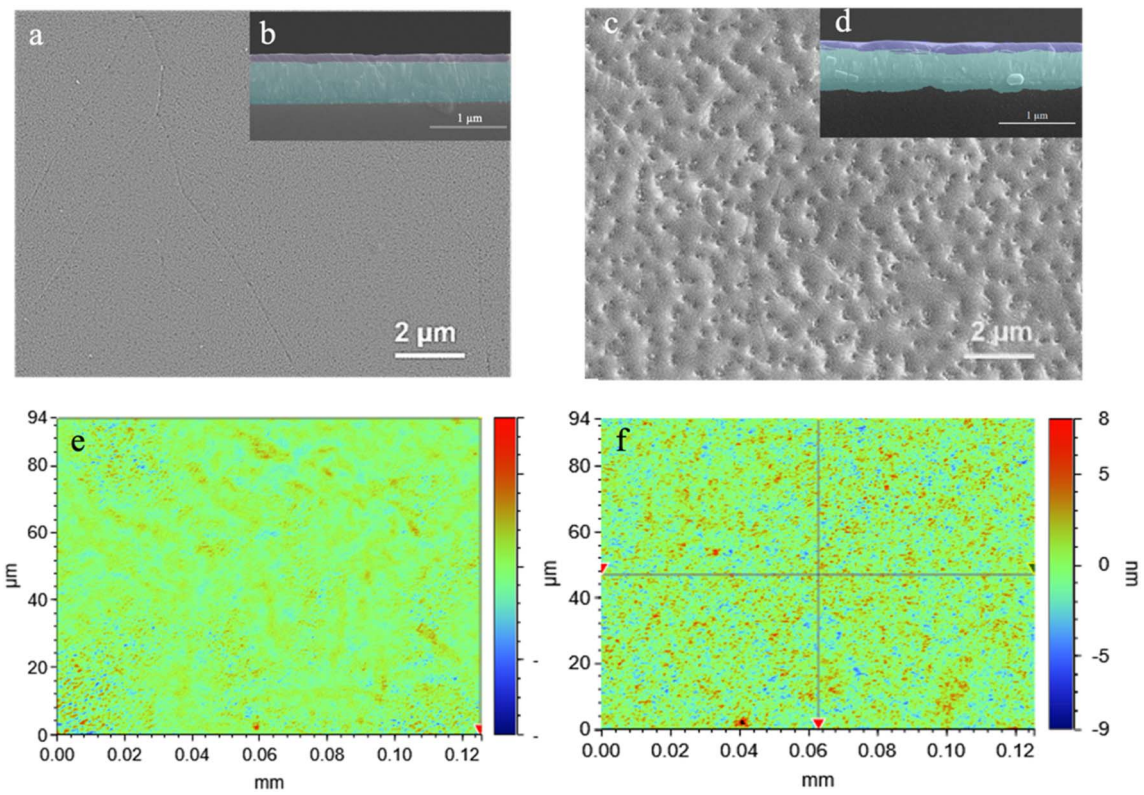

Fig. 3 SEM micrographs in top-view and cross-section (inset) of (a and b) $Sb(Ac)_3$/TU and (c and d) $SbCl_3$/TU films. The following color code is used to label the consecutive layers: FTO glass (turquoise) and Sb_2S_3 (purple). Optical profilometer images of (e) $Sb(Ac)_3$/TU and (f) $SbCl_3$/TU films.

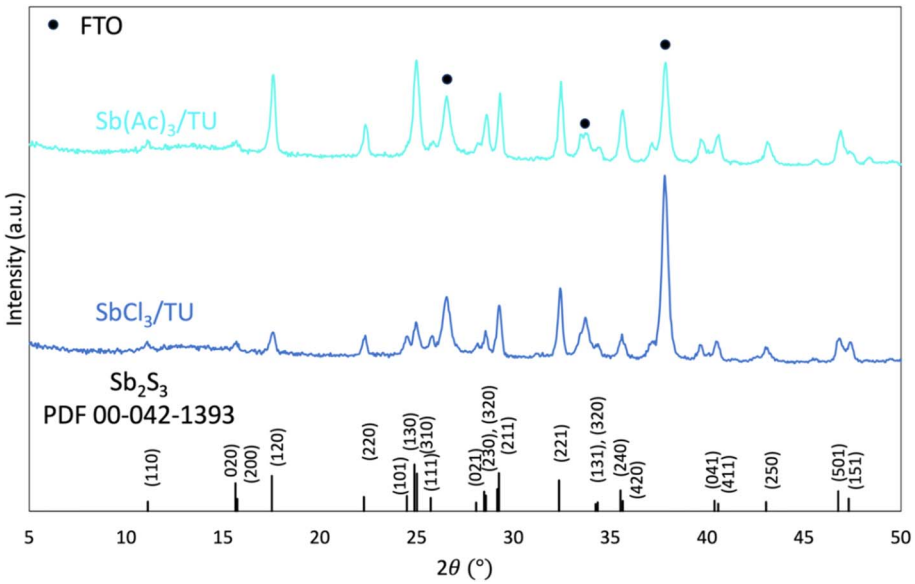

Fig. 4 X-ray diffractograms of Sb_2S_3 films from $Sb(Ac)_3$/TU (turquoise) and $SbCl_3$/TU (dark blue) solutions.

exhibit less coverage and less uniformity. The distinct morphologies of $Sb(Ac)_3$ and $SbCl_3$ films may stem from differences in their chemical properties. The acetate groups in $Sb(Ac)_3$ seem to provide molecular deformability, which could promote more homogeneous solvation and uniform nucleation during thin film formation. In contrast, $SbCl_3$ exhibits more heterogeneous interactions.[28] This difference may account for the smoother film obtained with $Sb(Ac)_3$. Further investigations, including theoretical studies, are necessary to validate these proposed molecular mechanisms. Optical profilometer measurements (Fig. 3e and f) corroborate the higher uniformity of $Sb(Ac)_3$/TU films with a lower R_q ($R_q = 1.19$ nm) compared to $SbCl_3$/TU films ($R_q = 2.01$ nm). For both films, the thickness is similar (~110 nm). As the charge diffusion length of stibine ranges between 30 and 300 nm, a layer thickness exceeding 300 nm may lead to increased recombination, reducing the efficiency of the solar cell.[29]

X-ray diffraction (XRD) measurements were performed on the Sb_2S_3 layers obtained from $Sb(Ac)_3$/TU and $SbCl_3$/TU solutions. Fig. 4 shows the XRD patterns of the stibine Sb_2S_3. We can observe that the Sb_2S_3 films formed from $Sb(Ac)_3$/TU and $SbCl_3$/TU are both crystalline. The Sb_2S_3 average crystallite size was calculated using the Scherrer equation on the most intense peak signals. No significant difference was observed between $Sb(Ac)_3$/TU and $SbCl_3$/TU samples, with extracted average values of 30 ± 4 nm and 28 ± 3 nm, respectively. As charge transport is anisotropic in Sb_2S_3, the solar cell performance should be linked to the crystalline orientation of the material. It was experimentally found that the most feasible orientation in Sb_2S_3 samples that allows rapid charge transport is the [*hk*1] orientation.[5,7]

The relative intensities and texture coefficients (Fig. 5a) were calculated to compare the preferred orientation of the films. Based on the relative intensities (eqn (3.1)), films formed from $Sb(Ac)_3$/TU show more intense peaks in the (120)> (130) > (221) > (211) > (420) planes whereas the films formed from the $SbCl_3$/TU precursor solution show more intense peaks for the (221) > (211) planes. The [*hk*1] orientation, necessary for improved charge transport, seems to be more prevalent in the $SbCl_3$/TU precursor.

$$\text{Relative intensity} = \frac{I(hkl)}{\sum_{i=1}^{N} I(hkl)} \tag{3.1}$$

where $I(hk\text{l})$ is the intensity of the diffraction peak of the *hkl* plane obtained in the measured diffractogram.

To probe the preferential orientation in the Sb_2S_3 films, the texture coefficient (TC) was used to normalize the experimental intensities based on simulated Sb_2S_3 intensities under the same measurement conditions. The TC was calculated from eqn (3.2):[30]

$$\text{TC}(hkl) = \frac{\dfrac{I(hkl)}{I_0(hkl)}}{\left[\dfrac{1}{N}\sum_{i=1}^{N}\dfrac{I(hkl)}{I_0(hkl)}\right]} \tag{3.2}$$

where $I(hkl)$ is the intensity of the diffraction peak of the *hkl* plane obtained from the measured diffractogram; $I_0(hkl)$ is the theoretical/simulated intensity of the diffraction peak obtained from PDF 00-042-1393 for the given *hkl* plane;[17,31–35] N is the number of considered*hkl* planes.

By convention, TC values greater than 1 indicate a preferential orientation of the considered crystalline planes.

To improve the data analysis accuracy, deconvolution was carried out when necessary, using Bruker software (DIFFRAC.TOPAS). The texture factor was calculated on peaks between 5 and 50°. Only a few peaks with very low intensity were neglected to minimize the error in the calculated values. A comparison of texture coefficients (Fig. 5b) for the two precursors shows that the (041) > (411) > (311) > (221) > (420) > (220)

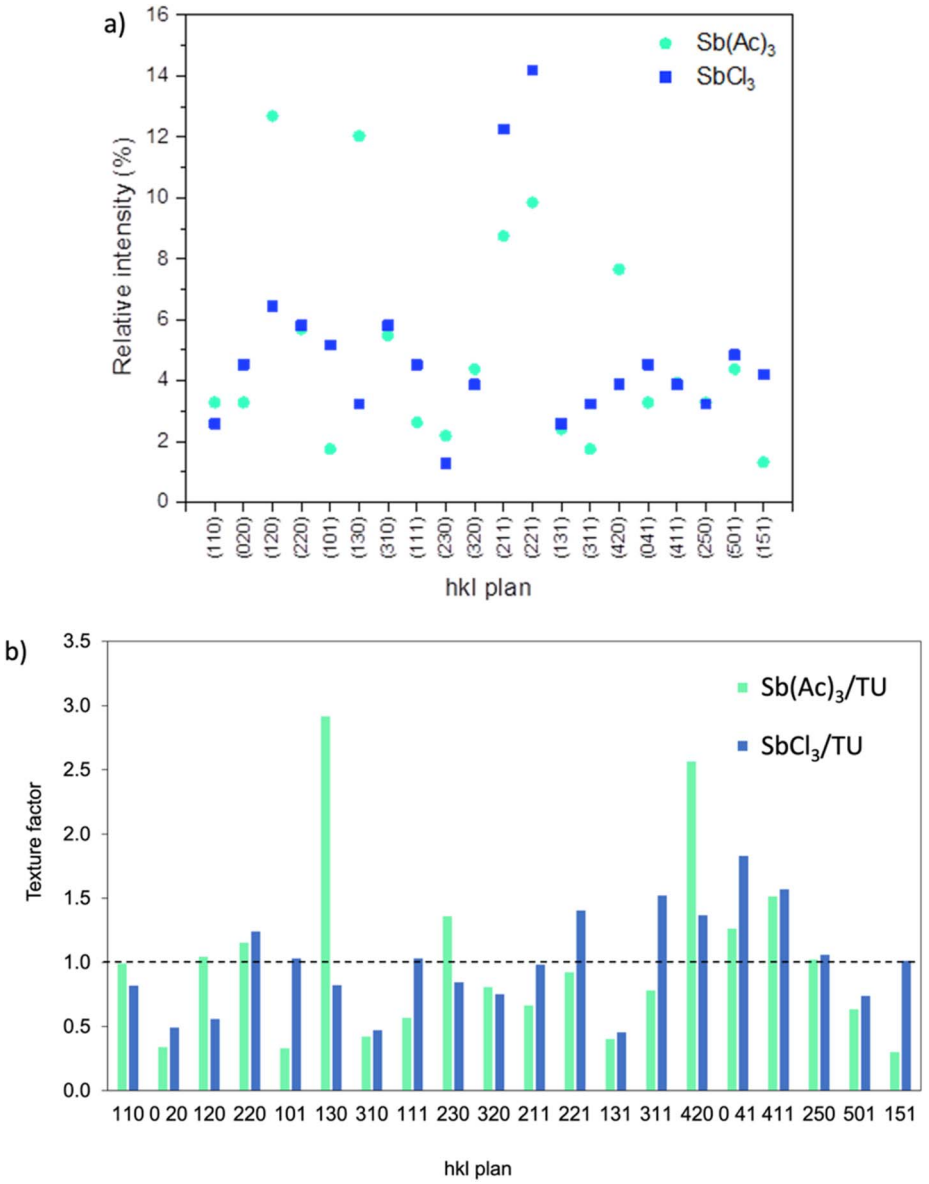

Fig. 5 (a) Relative intensity and (b) texture coefficients for different (*hkl*) planes of Sb_2S_3 films from $Sb(Ac)_3$/TU and $SbCl_3$/TU precursor solutions.

planes present a preferential orientation with TC values greater than 1 for samples obtained from $SbCl_3$/TU, whereas for samples obtained from $Sb(Ac)_3$/TU, the (130) > (420) > (411) > (230) > (041) > (220) planes are preferred. Thus, the [*hk*1] crystalline orientation of stibine is predominant in $SbCl_3$/TU films whereas [*hk*0] planes are more prevalent in $Sb(Ac)_3$/TU films.

A recent study showed that TiO_2 crystallization at 500 °C favors the matching of the crystal networks and bonding sites between TiO_2 and Sb_2S_3, facilitating [*hk*1] oriented growth.[10] In addition, the Sb_2S_3 samples studied here were annealed from a low temperature (100 °C) to a higher temperature (265 °C). This stabilization process should allow normal grain growth, favoring the presence of the [*hk*1] orientation (Fig. 2). The difference in crystalline orientation should therefore arise only from the precursors used as the thermal treatments for TiO_2 and Sb_2S_3 are the same. To the best of our knowledge, preferential orientation induced by the precursor nature has not been reported to date in the literature; this could help explain the differences in PV efficiency measured in full devices. From this point of view, $SbCl_3$/TU precursors give the best results.

3.1.2. Optical properties of Sb_2S_3 thin films. The optical absorbance spectra of $Sb(Ac)_3$/TU and $SbCl_3$/TU thin films are shown in Fig. 6. The absorbance is globally equivalent for both films in the range of solar spectrum radiation. $Sb(Ac)_3$/TU films absorb more below ~570 nm but less above ~570 nm compared to $SbCl_3$/TU films. Tauc plots allow the determination of a direct bandgap of ~1.65 and ~1.75 eV respectively for $SbCl_3$/TU and $Sb(Ac)_3$/TU samples, which are in accordance with the ones previously reported in the literature under similar synthesis conditions.[4,5] Reducing the bandgap from 1.75 eV to 1.65 eV can improve photovoltaic efficiency by broadening the absorption

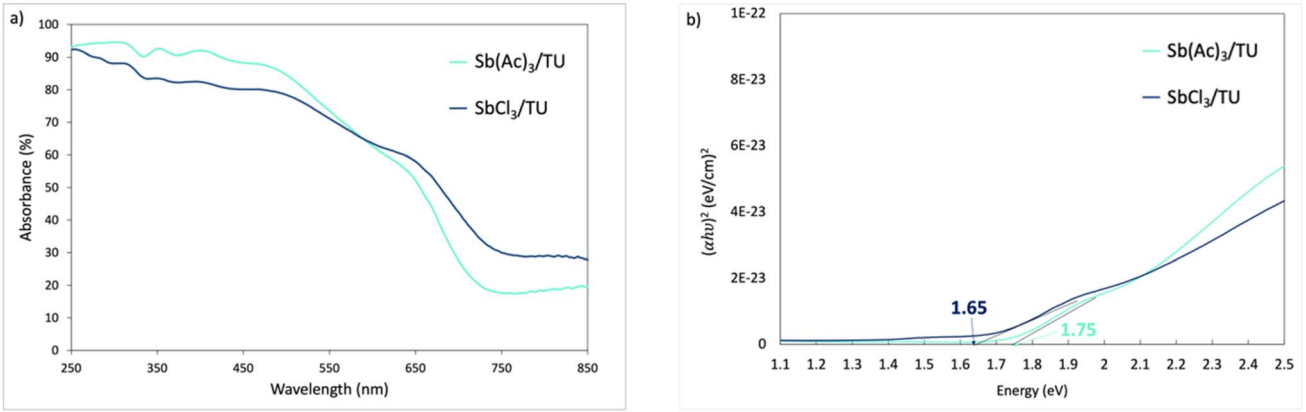

Fig. 6 (a) Absorbance spectra of Sb_2S_3 films from $Sb(Ac)_3$/TU (turquoise) and $SbCl_3$/TU (dark blue) precursor solutions. (b) Tauc plots of Sb_2S_3 films from $Sb(Ac)_3$/TU (turquoise) and $SbCl_3$/TU (dark blue) precursor solutions.

Table 2 Photovoltaic parameters of the best Sb_2S_3-based solar cells

	Direct				Reverse			
Solution	V_{oc} (V)	J_{sc} (mA cm^{-2})	FF	PCE (%)	V_{oc} (V)	J_{sc} (mA cm^{-2})	FF	PCE (%)
$SbCl_3$–TU	0.531	16.2	43	3.7	0.551	17.5	50	4.8
$Sb(Ac)_3$–TU	0.539	16.1	43	3.8	0.567	17.1	49	4.9

Table 3 Photovoltaic parameters of the Sb_2S_3-based solar cells (average of 20 devices)

		Direct				Reverse			
Solution		V_{oc} (V)	J_{sc} (mA cm^{-2})	FF	PCE (%)	V_{oc} (V)	J_{sc} (mA cm^{-2})	FF	PCE (%)
$SbCl_3$–TU	$\langle M \rangle$	0.487	16.1	44	3.5	0.523	15.8	49	4.1
	σ	0.020	1.2	2	0.4	0.019	1.1	2	0.5
$Sb(Ac)_3$–TU	$\langle M \rangle$	0.533	15.1	41	3.5	0.560	16.7	46	4.4
	σ	0.010	1.0	1	0.3	0.010	0.7	2	0.4

spectrum, enabling the material to absorb more photons, particularly in the visible range. The result is a higher short-circuit current density (J_{sc}). The optimized bandgap strikes an ideal balance between open-circuit voltage (V_{oc}) and J_{sc}, improving both without sacrificing either. Additionally, the narrower bandgap improves charge collection efficiency by reducing recombination losses and enhancing charge transport, as energy alignment at the interfaces is more favorable for carrier extraction, increasing overall device performance.

3.1.3. Assembly and characterization of Sb_2S_3 double perovskite solar cells. The PV performances of Sb_2S_3 films prepared from $Sb(Ac)_3$/TU and $SbCl_3$/TU were evaluated in devices assembled with the following architecture: glass/FTO/c-TiO_2/Sb_2S_3/spiro-OMeTAD/Au. The PCEs reported in this work (Tables 2 and 3) are similar for both precursor solutions, *i.e.*, $Sb(Ac)_3$/TU and $SbCl_3$/TU, and are in the upper range of efficiencies published to date (between 2.3% and 6.9%; Table 1) for spin-coated Sb_2S_3 as a photoactive material.[12,14–16,18–23,32] The $Sb(Ac)_3$/TU device tends to show a slightly enhanced V_{oc} of 0.567 V (average: 0.560 ± 0.010 V) *vs.* 0.551 V (average: 0.523 ± 0.19 V) for $SbCl_3$/TU device. Indeed, the more uniform and coverage-enhanced $Sb(Ac)_3$/TU film can reduce recombination in devices. Fewer electrons are trapped in the intermediate energy levels, which further results in an increased open circuit potential. The J_{sc} values are slightly higher for $SbCl_3$/TU devices in comparison with $Sb(Ac)_3$/TU corresponding to a slightly more efficient charge transfer into the selective contact. This difference in J_{sc} values could be due to a better [*hk*1] orientation and so a better charge transport within the layers, leading to improved charge collection at the electron selective contact and thus increased J_{sc}.

To further analyze the charge transfer properties of the $Sb(Ac)_3$/TU and $SbCl_3$/TU-based solar cells, EIS analyses were conducted, with results presented as Nyquist plots in Fig. 7. Data were fitted with the equivalent circuit model shown in the inset and are summarized in Table 4.[36–38]

The equivalent electrical circuit consists of a resistance R_1 (at high frequency), corresponding to the distance between the point (0, 0) and the intersection of the first semicircle with the *x*-axis,

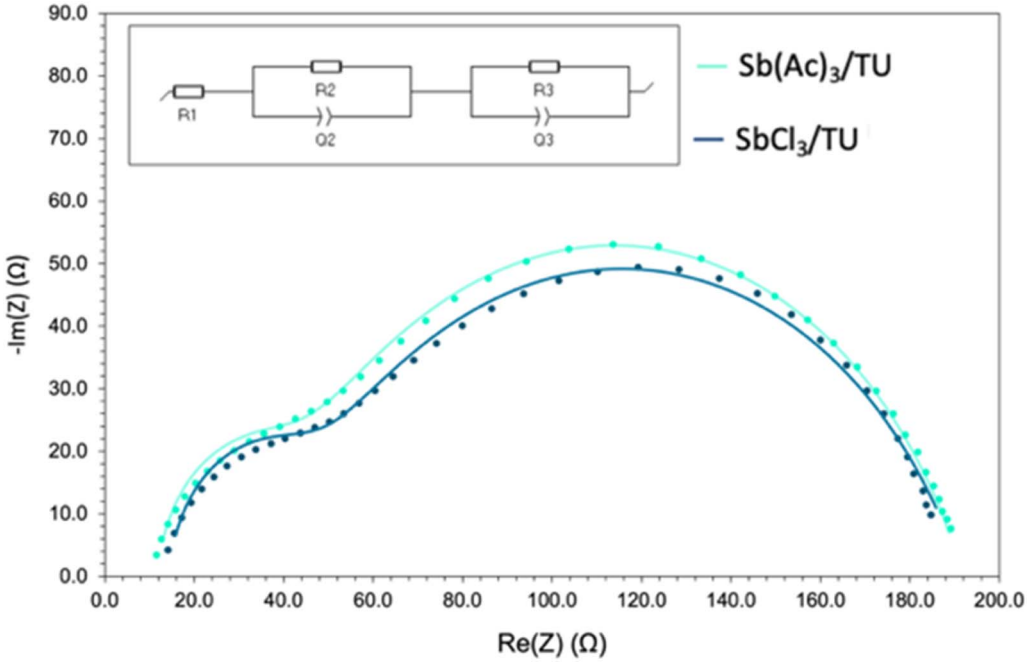

Fig. 7 EIS Nyquist plots of $Sb(Ac)_3$/TU (turquoise) and $SbCl_3$/TU (dark blue) Sb_2S_3-based solar cells; inset: the equivalent electrical circuit used for data fitting.

Table 4 Fitting resistance (R) and constant phase element (Q) parameters obtained from EIS data measured for $Sb(Ac)_3$/TU and $SbCl_3$/TU Sb_2S_3-based solar cells

	PCE (%)	R_1 [Ω]	Q_2 [10^{-3} F s^{a-1}]	a	R_2 [Ω]	Q_3 [10^{-6} F s^{b-1}]	b	R_3 [Ω]
$Sb(Ac)_3$–TU	4.9%	15	8.64	1	32	1.415	0.746	169
$SbCl_3$–TU	4.8%	14	11.51	1	28	2.075	0.732	150

which represents the series resistance (R_S). This resistance is associated with wires and contacts. The second elements $R_2//Q_2$ are described by the first semicircle, at medium frequency. They give information about the charge transfer at the interfaces between Sb_2S_3/HTL and/or TiO_2/Sb_2S_3. The $R_3//Q_3$ elements at low frequency are related to electron–hole interfacial recombination.

From data fitting (Table 4), the interfacial recombination resistance R_3 of the $Sb(Ac)_3$/TU device is 169 Ω, which is higher than the R_3 value of the $SbCl_3$/TU device (150 Ω). As the recombination rate is inversely proportional to R_3, it reveals lower interfacial recombination in the $Sb(Ac)_3$/TU device. This is more likely due to the more uniform film formed by the $Sb(Ac)_3$/TU precursors. Furthermore, the Q_3 value is higher for the $SbCl_3$/TU device which means a higher accumulation of charge at the interface, which is less favorable for PV devices. This is in agreement with the V_{oc} values obtained for the devices, as higher interfacial recombination and charge accumulation at the interface increase the forward bias diffusion current, which in turn reduces the open-circuit voltage.[39]

Looking at the R_2 charge transfer resistance to the selective contacts, we determined a slightly lower R_2 value for $SbCl_3$/TU (28 Ω) compared to the $Sb(Ac)_3$/TU (32 Ω) device, corresponding to a slightly more efficient charge transfer into the selective contact for the $SbCl_3$/TU device and so a higher J_{sc} value. This difference in J_{sc} values could be due to a better [$hk1$] orientation and so a better charge transport within the layers, leading to improved charge collection at the electron selective contact and thus increased J_{sc}. The EIS data thus globally corroborate J–V results.

This study shows that the $Sb(Ac)_3$/TU precursor solution produces films with better coverage and uniformity than films obtained from the $SbCl_3$/TU precursor solution. We would therefore expect to obtain better PV efficiencies for devices assembled from these films compared with those from $SbCl_3$/TU. However, the bandgap value (1.75 eV) is less favorable than for $SbCl_3$/TU (1.65 eV). In addition, the crystalline orientation [$hk0$] is more prevalent in $Sb(Ac)_3$/TU films, which does not favor efficient charge transfer in the devices. The preferential [$hk0$] orientation – *i.e.* parallel to the Sb_2S_3/TiO_2 interface – of $Sb(Ac)_3$/TU films could probably explain their better uniformity and coverage. Further study of the heat treatment and Sb : S ratio for films obtained with $Sb(Ac)_3$/TU precursors could be beneficial to improve efficiencies through fine tuning of the band gap and [$hk1$] crystalline orientation. All in all, a combination of three key factors can be highlighted to increase the efficiency of the assembled devices: uniformity and coverage of the photoactive layer, an adequate bandgap and a preferred [$hk1$] crystalline orientation.

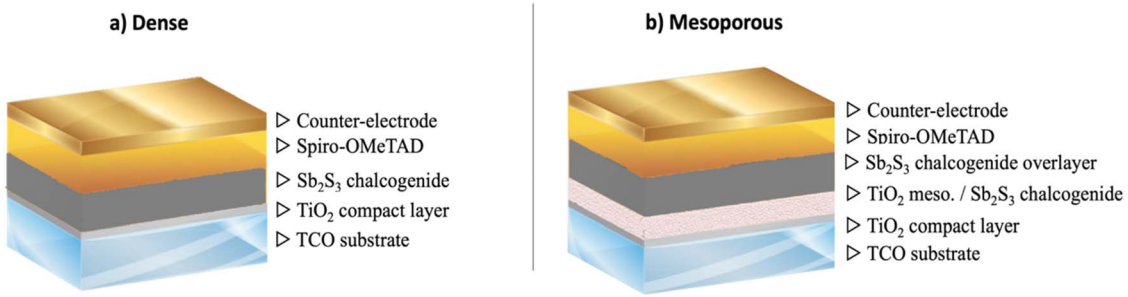

Fig. 8 Scheme of (a) dense and (b) mesoporous architectures of Sb_2S_3 devices.

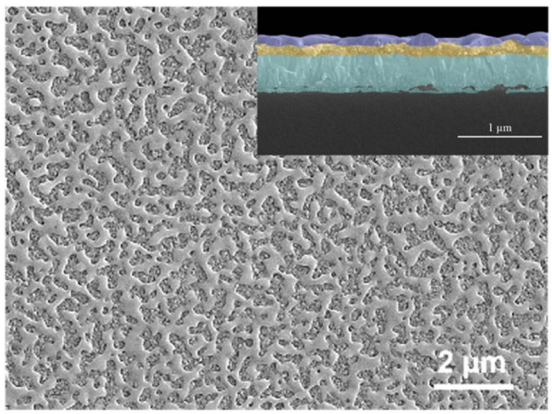

Fig. 9 SEM micrographs in top-view and cross-section (inset) of glass/FTO/c-TiO_2/mp-TiO_2/Sb_2S_3 sample. The following color code is used to label the consecutive layers: FTO glass (turquoise), c-TiO_2 and mp-TiO_2 (yellow) infiltrated by Sb_2S_3, and overlayer of Sb_2S_3 (purple).

3.2. Effect of the cell architecture in Sb_2S_3 devices

3.2.1. Structure and morphology of Sb_2S_3 thin films. In the first part of this study, tests were carried out with a dense layer of TiO_2 as the ETL (Fig. 8a). Alternatively, a stibine-infiltrated mesoporous TiO_2 layer can be incorporated on top of the dense TiO_2 layer in the device stack (Fig. 8b). This architecture is designed to increase the quantity of photoactive material while maintaining efficient charge diffusion and separation in the devices thanks to ETL/Sb_2S_3 interpenetration, thus boosting PV efficiencies. The two following device architectures (Fig. 8) with $SbCl_3$/TU as stibine precursors are then compared: glass/FTO/c-TiO_2/Sb_2S_3/spiro-OMeTAD/Au (referred to as the "dense" architecture) *vs.* glass/FTO/c-TiO_2/mp-TiO_2/Sb_2S_3/spiro-OMeTAD/Au (referred to as the "mesoporous" architecture).

SEM micrographs show that the substrate is not completely covered with stibine and is less uniformly covered in the mesoporous architecture than in the dense one. Small clusters appear to be deposited onto the mesoporous TiO_2 surface, which is visible below. From the cross-section micrographs, it is not possible to see if the stibine is infiltrated into the mesoporous TiO_2 network (Fig. 9). The aim of mesoporous TiO_2 is to increase the interaction interface with the stibine, thereby increasing charge separation and promoting electron collection and transport into the TiO_2 network, ultimately increasing cell efficiency.

To verify the infiltration of Sb_2S_3 into the mp-TiO_2, an XPS profile analysis was carried out (Fig. 10). The XPS profiles obtained for the glass/FTO/c-TiO_2/Sb_2S_3 sample (Fig. 10a) are presented and used as a reference to confirm the trends observed in the XPS analysis carried out on the glass/FTO/c-TiO_2/mp-TiO_2/Sb_2S_3 sample (Fig. 10b).

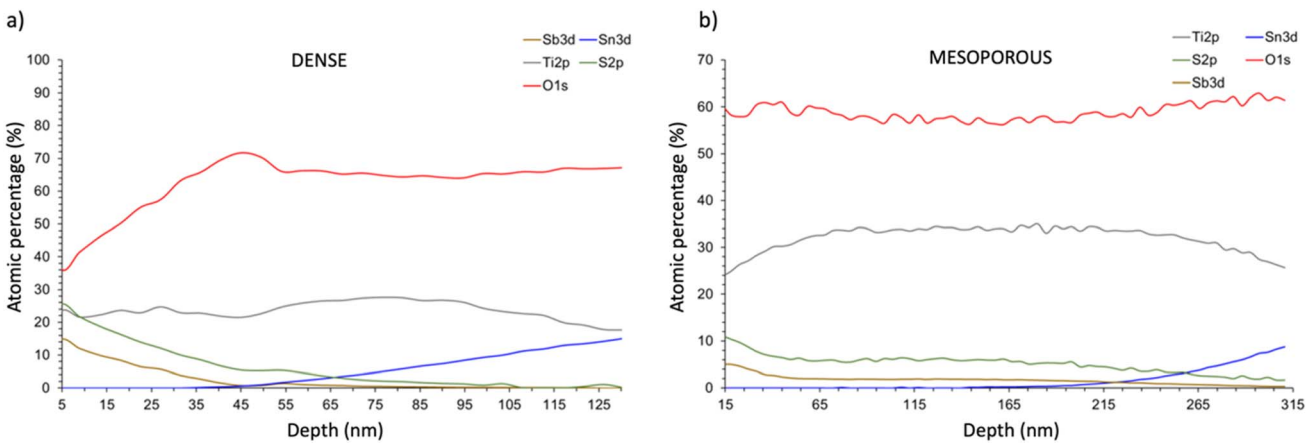

Fig. 10 XPS profiles for (a) glass-FTO/c-TiO_2/Sb_2S_3 and (b) glass-FTO/c-TiO_2/mp-TiO_2/Sb_2S_3 samples.

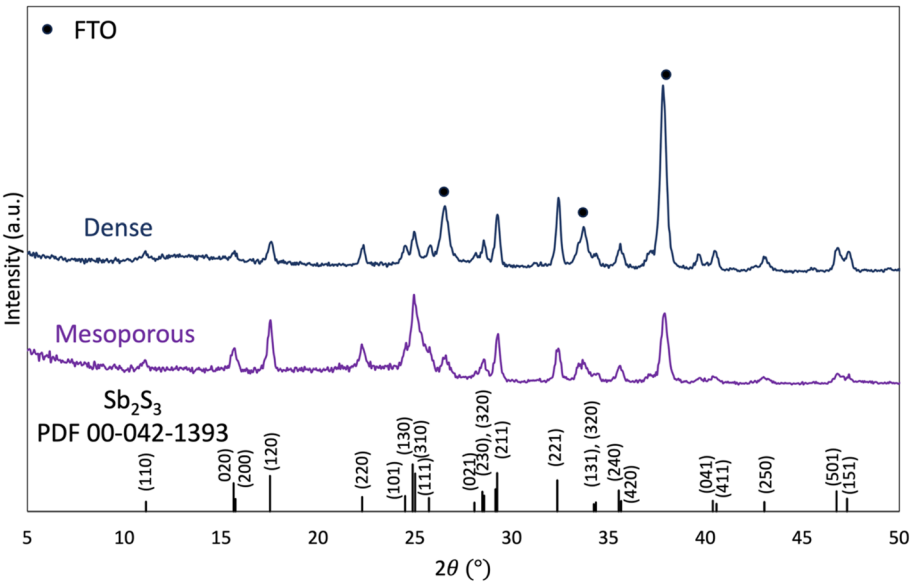

Fig. 11 X-ray diffractograms of glass-FTO/c-TiO_2/Sb_2S_3 (dark blue) and glass-FTO/c-TiO_2/mp-TiO_2/Sb_2S_3 (purple) samples.

In the "dense" sample (only c-TiO_2) XPS profile (Fig. 10a), the initial atomic percentages of sulfur and antimony are 26 and 15% respectively. Titanium is also present at an atomic percentage of 24% because the stibine film does not completely cover the surface of the glass/FTO/c-TiO_2 substrate. As the analysis depth increases, the atomic percentages of sulfur and antimony decrease, reaching zero at around 115 nm, as expected from the film thickness observed by SEM. However, the tin characteristic of FTO glass appears at values of 50 nm. As the substrate is not completely covered with stibine, it is possible for the ion beam to reach the FTO glass faster.

From the "mesoporous" sample (c-TiO_2 and mp-TiO_2) XPS profile (Fig. 10b), the atomic percentages of antimony and sulfur were determined to be 5% and 11%, respectively. This percentage corresponds to the stibine above the mesoporous TiO_2 layer. A titanium percentage of around 23% was also determined. As observed in the SEM micrographs, the stibine layer does not completely cover the substrate, leaving the mp-TiO_2 "visible". Between 15 and 55 nm depth, a slight decrease in atomic percentage is observed for antimony and sulfur, while the atomic percentage of titanium increases. This observation corresponds to interactions of the electron beam at the mp-TiO_2/Sb_2S_3 interface. Between 55 and 175 nm, the atomic percentage of the various elements remains constant, indicating the presence of both TiO_2 and Sb_2S_3. Finally, beyond 175 nm, the atomic percentage of sulfur and antimony decreases slightly, while that of TiO_2 remains constant, corresponding to the arrival of the beam on the dense TiO_2 layer. Next, the tin signal, which was zero until then, appears, indicating that the beam reaches the FTO glass substrate. The XPS profile therefore corroborates the infiltration of Sb_2S_3 into mp-TiO_2.

The diffractograms for both architectures (dense and mesoporous) were then compared (Fig. 11) and we can observe that Sb_2S_3 films are crystallized in both cases.

The calculation of the relative intensities (Fig. 12a, eqn (3.1)) highlights the planes with the highest intensity. For the mesoporous architecture, the peaks corresponding to the (310) and (120) planes have the highest intensity, followed by the (211), (220) and (221) planes, whereas for the dense architecture, the (221) and (211) planes are predominant, followed by the (120) and (310) planes. The texture factor TC (eqn (3.2)) was also calculated for both samples. The comparison of the texture coefficients (Fig. 12b) for the two architectures shows that the (041) > (411) > (311) > (221) > (220) planes have TC greater than 1 in "dense" devices, whereas for "mesoporous" devices, the (220) > (110) > (310) >(120) > (130) > (420) > (230) planes show preferred orientation. This suggests that glass/FTO/c-TiO_2/mp-TiO_2/Sb_2S_3 films have a preferential [*hk*0] orientation, whereas glass/FTO/c-TiO_2/Sb_2S_3 films have a preferential [*hk*1] orientation, with the latter showing improved charge transport. This misorientation in the mesoporous device could be caused by the confinement of Sb_2S_3 crystals within the mesoporous TiO_2 network. Indeed, in some studies,[38–40] larger pores (50–60 nm VS 25 nm for our study) were used, resulting in higher PV efficiencies (from 5.1% to 7.5% *vs.* 2.3% for our devices). However, in these studies, the orientation of the crystals was not verified, which underlines the importance of our preliminary work. Moreover, larger pores allow the growth of larger TiO_2 crystallites in the walls of the porous network, which has been reported to be critical for promoting [*hk*1] quasi-epitaxial growth at the Sb_2S_3/TiO_2 interface. In the mesoporous TiO_2 layer implemented in this paper, the crystallite size is around 15 nm and can reach 30–40 nm in a larger pore network, as we have already observed in other research conducted at GREEnMat aiming at the synthesis of an opal-like porous TiO_2 network by hard templating, using polystyrene beads as a sacrificial structuring agent.[37] This could explain the difference in results observed in previous studies.[40–42]

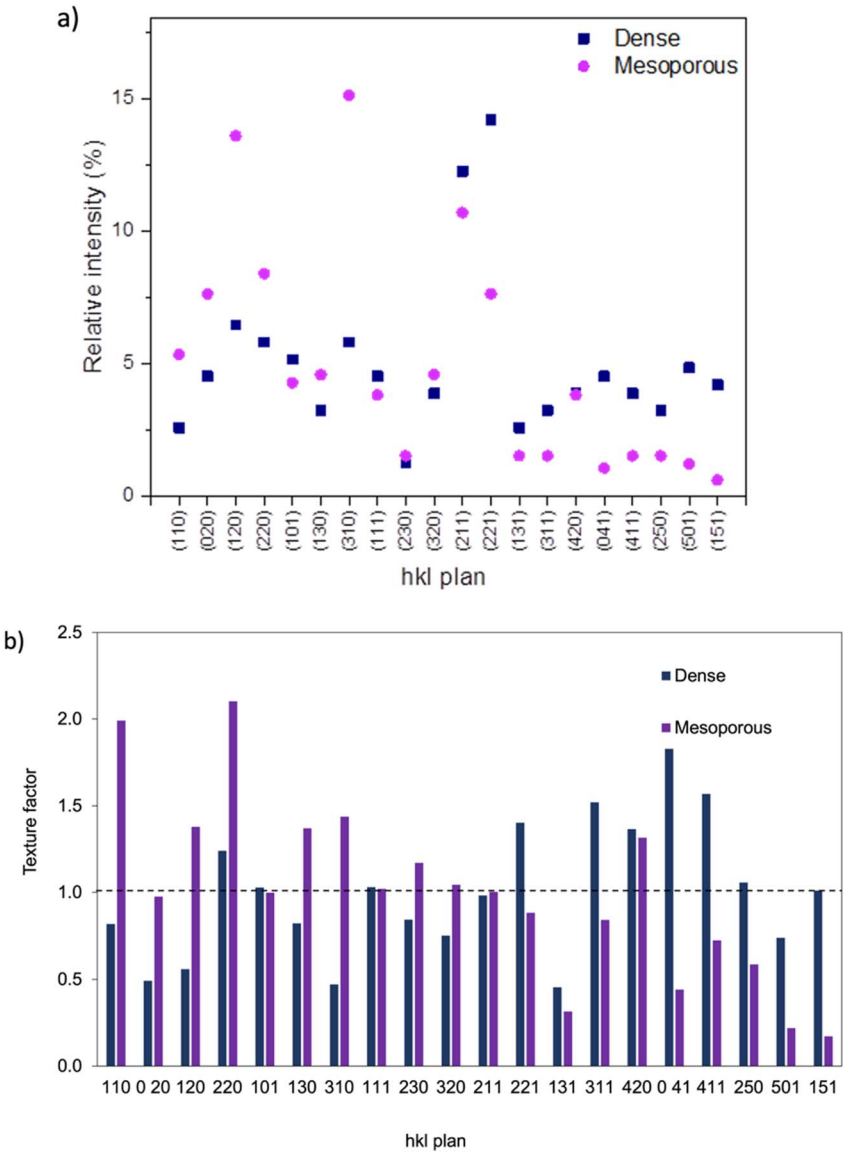

Fig. 12 (a) Relative intensity and (b) texture coefficients for different (*hkl*) planes of glass/FTO/c-TiO_2/Sb_2S_3 (dark blue) and glass/FTO/c-TiO_2/mp-TiO_2/Sb_2S_3 (purple) samples.

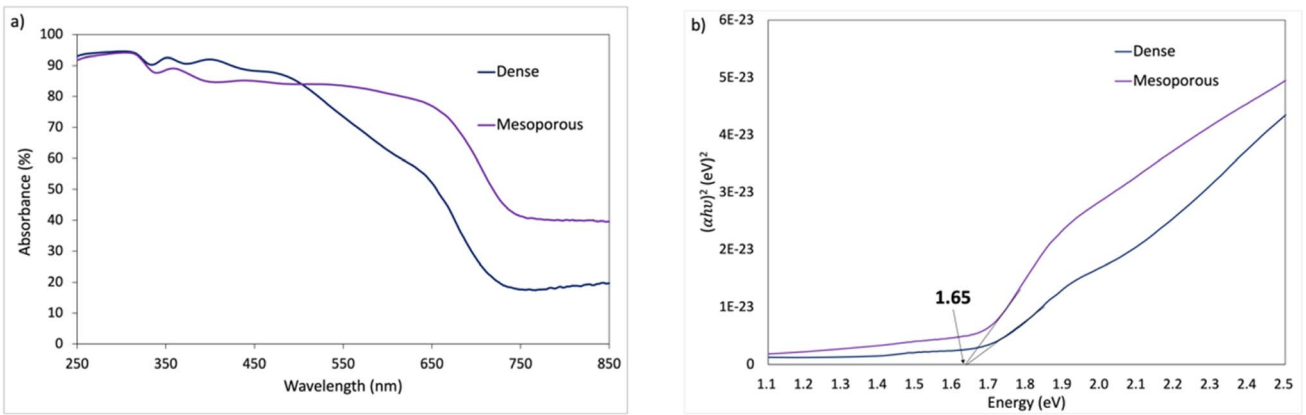

Fig. 13 (a) Absorbance spectra and (b) Tauc plots of glass/FTO/c-TiO_2/Sb_2S_3 (dark blue) and glass/FTO/c-TiO_2/mp-TiO_2/Sb_2S_3 (purple) samples.

Table 5 Photovoltaic parameters of the best Sb_2S_3-based solar cells

	Solar simulator							
	Direct				Inverse			
Sample	V_{oc} (V)	J_{sc} (mA cm^{-2})	FF	PCE (%)	V_{oc} (V)	J_{sc} (mA cm^{-2})	FF	PCE (%)
Dense	0.531	16.2	43	3.7	0.551	17.5	50	4.8
Mesoporous	0.536	10.3	40	2.2	0.548	8.5	49	2.3

Table 6 Photovoltaic parameters of the Sb_2S_3-based solar cells (average of 20 devices)

		Solar simulator							
		Direct				Inverse			
Sample		V_{oc} (V)	J_{sc} (mA cm^{-2})	FF	PCE (%)	V_{oc} (V)	J_{sc} (mA cm^{-2})	FF	PCE (%)
Dense	$\langle M \rangle$	0.487	16.1	44	3.5	0.523	15.8	49	4.1
	σ	0.020	1.2	2	0.4	0.019	1.1	2	0.5
Mesoporous	$\langle M \rangle$	0.493	9.5	38	1.8	0.507	8.1	44	1.9
	σ	0.038	0.7	4	0.4	0.037	0.5	5	0.4

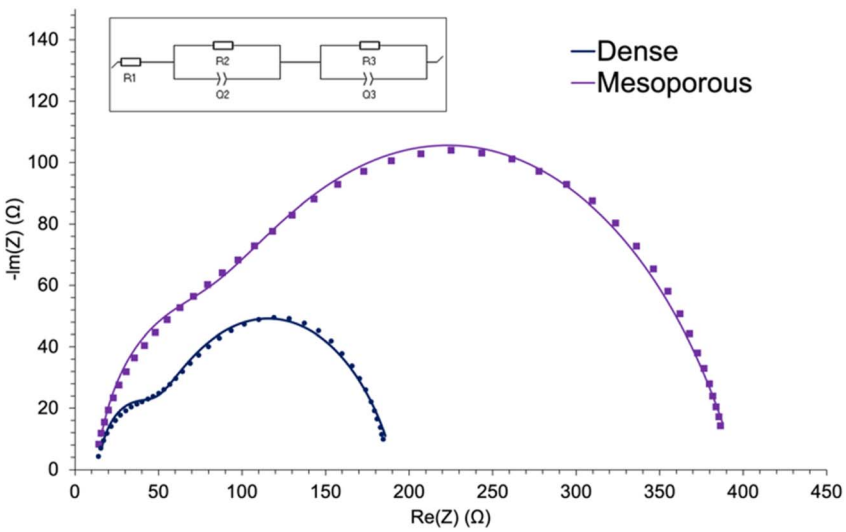

Fig. 14 EIS Nyquist plots of glass/FTO/c-TiO_2/Sb_2S_3/spiro/Au (dark blue) and glass/FTO/c-TiO_2/mp-TiO_2/Sb_2S_3/spiro/Au (purple) solar cells; inset: the equivalent electrical circuit used for data fitting.

3.2.2. Optical properties of Sb_2S_3 thin films. The optical absorbance spectra of glass/FTO/c-TiO_2/Sb_2S_3 and glass/FTO/c-TiO_2/mp-TiO_2/Sb_2S_3 samples are shown in Fig. 13. The absorbance is generally higher in the mesoporous architecture. This is due to the higher quantity of stibine material, *i.e.* infiltrated into the mesoporous TiO_2 and in the overlayer at the surface of the TiO_2 mesoporous network. Tauc plots allow the determination of a direct bandgap of ~1.65 eV for both architectures. These values are in accordance with the ones previously reported in the literature under similar synthesis conditions.[4,29] Furthermore, it is obvious that the values are similar because the precursors and the deposition method are identical for both architectures. Only the heat treatment slightly varies from one architecture to the other.

3.2.3. Assembly and characterization of Sb_2S_3 double perovskite solar cells. The PV performances of the Sb_2S_3 solar cells were evaluated for the following architectures: glass/FTO/c-TiO_2/Sb_2S_3/spiro-OMeTAD/Au (dense architecture) and glass/FTO/c-TiO_2/mp-TiO_2/Sb_2S_3/spiro-OMeTAD/Au (mesoporous architecture). The PCEs reported in this work (Tables 5 and 6) are much higher for the dense architecture in comparison with the mesoporous one (4.8% *vs.* 2.3%).

The "dense" device shows higher J_{sc} values (17.5 mA cm^{-2} (average: 16.1 ± 1.2 mA cm^{-2})) in comparison with the

Table 7 Fitting resistance (R) and constant phase element (Q) parameters obtained from EIS data measured on glass/FTO/c-TiO_2/Sb_2S_3/spiro/Au and glass/FTO/c-TiO_2/mp-TiO_2/Sb_2S_3/spiro/Au solar cells

	PCE (%)	R_1 [Ω]	Q_2 [10^{-3} F s^{a-1}]	a	R_2 [Ω]	Q_3 [10^{-6} F s^{b-1}]	b	R_3 [Ω]
Dense	4.8%	14	11.51	1	28	2.075	0.732	150
Mesoporous	2.3%	12	11.15	1	46	1.820	0.702	339

mesoporous architecture (8.5 mA cm^{-2} (average: 8.1 ± 0.5 mA cm^{-2})). The Sb_2S_3 film exhibits slightly better coverage and uniformity in the dense architecture. However, the amount of material is significantly higher in the mesoporous architecture. The literature states that a thickness between 30 and 300 nm is appropriate considering the diffusion length of electrons within the Sb_2S_3.[29] In addition, mesoporous TiO_2 should increase the interaction interface with Sb_2S_3, and thus increase the charge transfer paths between these two materials. But more importantly, it appears that glass/FTO/c-TiO_2/mp-TiO_2/Sb_2S_3 films have a preferential [hk0] orientation, whereas glass/FTO/c-TiO_2/Sb_2S_3 films have a preferential [hk1] orientation.

The decrease in efficiency is therefore mainly due to the [hk0] misorientation of the stibine crystals in the mesoporous architecture, resulting in poor charge transport and hence the observed decrease in J_{sc}.

To further analyze the charge transfer properties of "dense" and "mesoporous" solar cells, EIS analyses were conducted. Results are presented as Nyquist plots in Fig. 14. Data were fitted with the equivalent circuit model (inset) and are summarized in Table 7.

A lower R_2 value is obtained for the dense architecture (28 Ω) compared to the mesoporous (46 Ω) device, corresponding to a more efficient charge transfer at the selective contact in the "dense" device. Usually, in perovskite solar cells, the mesoporous TiO_2 improves charge collection, resulting in a lower resistance R_2 in the mesoporous architecture than in the dense one.[5,41] However, in the case of stibine, the crystalline orientation has a non-negligible influence. Indeed, the [hk1] orientation allows a better charge transport within layers, leading to improved charge collection at the electron selective contact and thus increased J_{sc} for the dense architecture.

The interfacial recombination resistance R_3 of the mesoporous device (339 Ω) is higher than the R_3 value of the dense device (150 Ω). As the recombination rate at the Sb_2S_3/spiro-OMeTAD interface is inversely proportional to R_3, it indicates faster interfacial recombination in the dense device. In addition, a higher Q_3 value is obtained in the dense device than in the mesoporous one, which means a higher accumulation of charges at the interface due to the absence of the mesoporous TiO_2 network, increasing the electron extraction interface between stibine and the ETL. Therefore, it can be assumed that more charges are transported into the stibine in the dense architecture thanks to its preferred [hk1] crystalline orientation; however the smaller interface between stibine and dense TiO_2 leads to an accumulation of charges that can then undergo recombination.

All in all, EIS measurements corroborate J–V curves and the [hk0] misorientation of the stibine crystals in the mesoporous architecture has the greatest impact on the device efficiency, through the decrease in J_{sc}.

4. Conclusion

Sb_2S_3 is a binary chalcogenide semiconductor which is abundant on Earth, stable, non-toxic, and inexpensive. Therefore, scientists are particularly interested in this compound for its excellent optoelectronic properties. Many studies have been carried out notably on the S/Sb ratio, concentrations, deposition speeds, doping, *etc.* However, no studies comparing different precursors for Sb_2S_3 stibine formation or the architecture (dense and mesoporous) of the assembled devices have been published to date.

This work reports for the first time the effect of the antimony precursor used for the Sb_2S_3 film formation and the architecture of the cells on the preferential orientation of the stibine crystals. Indeed, as stibine shows anisotropic charge transfer properties, its crystalline orientation can directly impact the efficiency of the devices. A [hk1] crystal orientation reduces recombination, improves charge transport and is therefore desired for efficient PV devices.

In the first part of this study, $Sb(Ac)_3$ and $SbCl_3$ were compared as antimony precursors. The $Sb(Ac)_3$/TU solution allows the formation of films with higher coverage and uniformity compared to those obtained from the $SbCl_3$/TU solution. However, from the perspective of PV efficiencies, it is not sufficient (4.9% and 4.8% respectively) because the bandgap of $Sb(Ac)_3$/TU (1.75 eV) is less favorable than that of $SbCl_3$/TU (1.65 eV). In addition, the [hk0] crystalline orientation is more prevalent in $Sb(Ac)_3$/TU films, which does not favor efficient charge transfer in the devices.

In the second part, the incorporation of a mesoporous TiO_2 network in the device stack was considered to increase the quantity of Sb_2S_3 photoactive material and improve the charge transfer in the devices. The morphology of the stibine (over) layer in both dense and mesoporous architectures is similar but slightly less covering in the case of mesoporous architecture, and it was proved that the stibine fills the TiO_2 mesoporous network. Moreover, the measured bandgaps are similar (1.65 eV). However, the PV efficiencies are significantly lower in the case of mesoporous architecture (2.3% *vs.* 4.8%), which can mainly be attributed to the [hk0] misorientation of the crystals leading to poor charge transport and therefore a decrease in J_{sc}.

This study highlights that a combination of three factors is crucial to boost Sb_2S_3-based device efficiencies: uniformity and coverage of the Sb_2S_3 layer, an adequate bandgap, and a [hk1] crystalline orientation. This work therefore proves that careful examination and fine-tuning of these three properties are

essential when working on Sb_2S_3-based solar cells and paves the way for further research in this area.

Data availability

The authors confirm that the data supporting the findings of this study are available within the article.

Conflicts of interest

The authors declare that they have no known competing financial interests or personal relationships that could have appeared to influence the work reported in this paper.

Acknowledgements

This work was supported by the Department of Chemistry of the University of Liège. The authors acknowledge Prof. Luc Henrard from the University of Namur for XPS measurements and the team members of GREEnMat for additional technical and administrative support.

References

1 M. A. Farhana, A. Manjceevan and J. Bandara, Recent advances and new research trends in Sb_2S_3 thin film based solar cells, *J. Sci.:Adv. Mater. Devices*, 2023, **8**(1), 100533.
2 S. Barthwal, R. Kumar and S. Pathak, Present Status and Future Perspective of Antimony Chalcogenide (Sb2X3) Photovoltaics, *ACS Appl. Energy Mater.*, 2022, **5**(6), 6545–6585.
3 U. A. Shah, S. Chen, G. M. G. Khalaf, Z. Jin and H. Song, Wide Bandgap Sb_2S_3 Solar Cells, *Adv. Funct. Mater.*, 2021, **31**(27), 2100265.
4 H. Deng, Y. Zeng, M. Ishaq, S. Yuan, H. Zhang, X. Yang, M. Hou, U. Farooq, J. Huang, K. Sun, R. Webster, H. Whu, Z. Chen, F. Yi, H. Song, X. Hao and J. Tang, Quasiepitaxy Strategy for Efficient Full-Inorganic Sb_2S_3 Solar Cells, *Adv. Funct. Mater.*, 2019, **29**(31), 1901720.
5 X. Jin, Y. Fang, T. Salim, M. Feng, S. Hadke, L. S. Woei, T. Chien Sum and L. H. Wong, In Situ Growth of [hk1]-Oriented Sb_2S_3 for Solution-Processed Planar Heterojunction Solar Cell with 6.4% Efficiency, *Adv. Funct. Mater.*, 2020, **30**(35), 2002887.
6 H. Ennaceri, M. Boujnah, A. Taleb, A. Khaldoun, R. Sáez-Araoz, A. Ennaoui, A. El Kenz and A. Benyoussef, Thickness effect on the optical properties of TiO_2 anatase thin films prepared by ultrasonic spray pyrolysis: Experimental and ab initio study, *Int. J. Hydrogen Energy*, 2017, **42**, 19467–19480.
7 Y. Zeng, K. Sun, J. Huang, M. P. Nielsen, F. Ji, C. Sha, S. Yuan, X. Zhang, C. Yan, X. Liu, H. Deng, Y. Lai, J. Seidel, N. Ekins-Daukes, F. Liu, H. Song, M. Green and X. Hao, Quasi-Vertically-Orientated Antimony Sulfide Inorganic Thin-Film Solar Cells Achieved by Vapor Transport Deposition, *ACS Appl. Mater. Interfaces*, 2020, **12**(20), 22825–22834.
8 C. Wu, L. Zhang, B. Che, P. Xiao, J. Yang, H. Wang, L. Chu, W. Yan and T. Chen, The role of grain growth in controlling the crystal orientation of Sb_2S_3 films for efficient solar cells, *J. Mater. Chem. A*, 2023, **11**(15), 8184–8191.
9 M. S. You, C.-S. Lim, D. H. Kwon, J. H. Heo, S. H. Im and K. J. Chae, Oxide-free Sb_2S_3 sensitized solar cells fabricated by spin and heat-treatment of Sb(III)(thioacetamide)$_2$Cl$_3$, *Org. Electron.*, 2015, **21**, 155–159.
10 Y. C. Choi and S. I. Seok, Efficient Sb_2S_3-sensitized solar cells via single-step deposition of Sb_2S_3 using S/Sb-ratio-controlled $SbCl_3$-thiourea complex solution, *Adv. Funct. Mater.*, 2015, **25**(19), 2892–2898.
11 E. K. Gil, S.-J. Lee, S.-J. Sung, K. Y. Cho and D.-H. Kim, Spin-Coating Process of an Inorganic Sb_2S_3 Thin Film for Photovoltaic Applications, *J. Nanosci. Nanotechnol.*, 2016, **16**(10), 10763–10766.
12 L. Zheng, K. Jiang, J. Huang, Y. Zhang, B. Bao, X. Zhou, H. Wang, B. Guan, L. M. Yang and Y. Song, Solid-state nanocrystalline solar cells with an antimony sulfide absorber deposited by an in situ solid–gas reaction, *J. Mater. Chem. A*, 2017, **5**(10), 4791–4796.
13 R. Tang, X. Wang, C. Jiang, S. Li, W. Liu, H. Ju, S. Yang, C. Zhu and T. Chen, n-Type Doping of Sb_2S_3 Light-Harvesting Films Enabling High-Efficiency Planar Heterojunction Solar Cells, *ACS Appl. Mater. Interfaces*, 2018, **10**(36), 30314–30321.
14 C. Jiang, R. Tang, X. Wang, H. Ju, G. Chen and T. Chen, Alkali Metals Doping for High- Performance Planar Heterojunction Sb_2S_3 Solar Cells, *Sol. RRL*, 2019, **3**(1), 1800272.
15 R. Tang, X. Wang, C. Jiang, S. Li, G. Jiang, S. Yang, C. Zhu and T. Chen, Vacuum assisted solution processing for highly efficient Sb_2S_3 solar cells, *J. Mater. Chem. A*, 2018, **6**(34), 16322–16327.
16 C. Guo, J. Chen, G. Li, X. Liang, W. Lai, L. Yang, Y. Mai and Z. Li, Enhanced Electrical Conductivity of Sb_2S_3 Thin Film via C_{60} Modification and Improvement in Solar Cell Efficiency, *Global Chall.*, 2019, **3**(7), 1800108.
17 M. Tamilselvan, A. Byregowda, C.-Y. Su, C.-J. Tseng and A. J. Bhattacharyya, Planar Heterojunction Solar Cell Employing a Single-Source Precursor Solution-Processed Sb_2S_3 Thin Film as the Light Absorber, *ACS Omega*, 2019, **4**(7), 11380–11387.
18 J. Han, S. Wang, J. Yang, S. Guo, Q. Cao, H. Tang, X. Pu, B. Gao and X. Li, Solution-Processed Sb_2S_3 Planar Thin Film Solar Cells with a Conversion Efficiency of 6.9% at an Open Circuit Voltage of 0.7 V Achieved via Surface Passivation by a SbCl $_3$ Interface Layer, *ACS Appl. Mater. Interfaces*, 2020, **12**(4), 4970–4979.
19 S. Wang, Y. Zhao, B. Che, C. Li, X. Chen, R. Tang, J. Gong, X. Wang, G. Chen, T. Chen, J. Li and X. Xiao, A Novel Multi-Sulfur Source Collaborative Chemical Bath Deposition Technology Enables 8%-Efficiency Sb_2S_3 Planar Solar Cells, *Adv. Mater.*, 2022, **34**(41), 2206242.
20 Y. C. Choi, D. U. Lee, J. H. Noh, E. K. Kim and S. I. Seok, Highly improved Sb_2S_3 sensitized-inorganic-organic

heterojunction solar cells and quantification of traps by deep-level transient spectroscopy, *Adv. Funct. Mater.*, 2014, **24**(23), 3587–3592.

21 J. Zheng, C. Liu, L. Zhang, Y. Chen, F. Bao, J. Liu, H. Zhu, K. Shen and Y. Mai, Enhanced hydrothermal heterogeneous deposition with surfactant additives for efficient Sb_2S_3 solar cells, *Chem. Eng. J.*, 2022, **446**, 136474.

22 Y. Li, R. Li, Z. Jia, B. Yu, Y. Yang, S. Bai, M. Pollard, Y. Liu, Y. Ma, H. Kampwerth and Q. Lin, Precursor Engineering of Solution-Processed Sb_2S_3 Solar Cells, *Small*, 2024, **20**(10), 2308895.

23 A. Maiti, S. Chatterjee and A. J. Pal, Sulfur-Vacancy Passivation in Solution-Processed Sb_2S_3 Thin Films: Influence on Photovoltaic Interfaces, *ACS Appl. Energy Mater.*, 2020, **3**(1), 810–821.

24 L. Zhang, W. Lian, X. Zhao, Y. Yin, T. Chen and C. Zhu, Sb_2S_3 Seed-Mediated Growth of Low-Defect Sb_2S_3 on a TiO_2 Substrate for Efficient Solar Cells, *ACS Appl. Energy Mater.*, 2020, **3**(12), 12417–12422.

25 X. Wang, J. Li, W. Liu, S. Yang, C. Zhu and T. Chen, A fast chemical approach towards Sb_2S_3 film with a large grain size for high-performance planar heterojunction solar cells, *Nanoscale*, 2017, **9**(10), 3386–3390.

26 L. Zhu, J. Chen, R. Liu, C. Dong, S. Yang, T. Chen, C. Chen, Q. Qiao and M. Wang, Solution-Processed Compact Sb_2S_3 Thin Films by a Facile One-Step Deposition Method for Efficient Solar Cells, *Sol. RRL*, 2021, **5**(11), 2100666.

27 R. Kondrotas, C. Chen and J. Tang, Sb_2S_3 Solar Cells, *Joule*, 2018, **2**(5), 857–878.

28 S. M. Luz, J. Del Tio, G. J. M. Rocha, A. R. Gonçalves and A. P. Del'Arco, Cellulose and cellulignin from sugarcane bagasse reinforced polypropylene composites: Effect of acetylation on mechanical and thermal properties, *Composites, Part A*, 2008, **39**(9), 1362–1369.

29 Z. Li, X. Chen, H. Zhu, J. Chen, Y. Guo, C. Zhang, W. Zhang, X. Niu and Y. Mai, Sb_2Se_3 thin film solar cells in substrate configuration and the back contact selenization, *Sol. Energy Mater. Sol. Cells*, 2017, **161**, 190–196.

30 Y. Zhou, L. Wang, S. Chen, S. Qin, X. Liu, J. Chen, D. J. Xue, M. Luo, Y. Cao, Y. Chen, E. H. Sargen and J. Tang, Thin-film Sb_2Se_3 photovoltaics with oriented one-dimensional ribbons and benign grain boundaries, *Nat. Photonics*, 2015, **9**(6), 409–415.

31 S. Qiao, J. Liu, Z. Li, S. Wang and G. Fu, Sb_2S_3 thickness-dependent lateral photovoltaic effect and time response observed in glass/FTO/CdS/Sb_2S_3/Au structure, *Opt. Express*, 2017, **25**(16), 19583.

32 Z. Peng, Q. Zheng, R. Wang, L. Sun, H. Wang, Y. Yuan, Y. Xing, L. Yao, J. Bi and W. Li, Controllable (HK1) Preferred Orientation of Sb_2S_3 Thin Films Fabricated by Pulse Electrodeposition, *SSRN Electron. J.*, 2022, 112208.

33 K. Lv, C. Shi, Y. Yang, H. Fu, F. Guo and Q. Wang, The non-aqueous chemical bath deposition of Sb_2S_3 thin films using SbCl3-thioacetamide complex solution in DMF and the photovoltaic performance of the corresponding solar cells, *Mater. Lett.*, 2019, **256**, 126636.

34 R. Liu, C. Dong, L. Zhu, J. Chen, J. Huang, W. Cao, X. Zhang, C. Ge, S. Yang, T. Chen and M. Wang, Heteroepitaxial and homoepitaxial nucleation strategies to grow Sb_2S_3 nanorod arrays and therefrom a derived gain of 7.18%-efficient $Sb_2(S,Se)_3$ quasi- nanoarray heterojunction solar cells, *Appl. Mater. Today*, 2022, **27**, 101487.

35 L. Zhang, C. Wu, W. Liu, S. Yang, M. Wang, T. Chen and C. Zhu, Sequential deposition route to efficient Sb_2S_3 solar cells, *J. Mater. Chem. A*, 2018, **6**(43), 21320–21326.

36 N. Daem, J. Dewalque, F. Lang, A. Maho, G. Spronck, C. Henrist, P. Colson, S. D. Stranks and R. Cloots, Spray-Coated Lead-Free $Cs_2AgBiBr_6$ Double Perovskite Solar Cells with High Open-Circuit Voltage, *Sol. RRL*, 2021, **5**(9), 2100422.

37 A. Maho, M. Lobet, N. Daem, P. Piron, G. Spronck, J. Loicq, R. Cloots, P. Colson, C. Henrist and J. Dewalque, Photonic Structuration of Hybrid Inverse-Opal TiO_2 Perovskite Layers for Enhanced Light Absorption in Solar Cells, *ACS Appl. Energy Mater.*, 2021, **4**(2), 1108–1119.

38 N. Daem, J. Dewalque, D. K. Kim, G. Spronck, M. Attwood, J. Wade, C. Henrist, P. Colson, S. Heutz, R. Cloots and A. Maho, Improved Photovoltaic Performances of Lead-Free $Cs_2AgBiBr_6$ Double Perovskite Solar Cells Incorporating Tetracene as Co-Hole Transport Layer, *Sol. RRL*, 2023, **7**(17), 2300391.

39 W. Tress, K. Leo and M. Riede, Optimum mobility, contact properties, and open-circuit voltage of organic solar cells: A drift-diffusion simulation study, *Phys. Rev. B:Condens. Matter Mater. Phys.*, 2012, **85**(15), 1–11.

40 J. A. Chang, J. H. Rhee, I. S. Hyuk, Y. H. Lee, H.-J. Kim, S. Seok, M. K. Nazeeruddin and M. Grätzel, High-performance nanostructured inorganic-organic heterojunction solar cells, *Nano Lett.*, 2010, **10**(7), 2609–2612.

41 K. C. Gödel, Y. Chan Choi, B. Roose, A. Sadhanala, H. J. Snaith, S. I. Seok, U. Steiner and S. K. Pathak, Efficient room temperature aqueous Sb_2S_3 synthesis for inorganic-organic sensitized solar cells with 5.1% efficiencies, *Chem. Commun.*, 2015, **51**(41), 8640–8643.

42 Y. C. Choi, D. U. Lee, J. H. Noh, E. K. Kim and S. I. Seok, Highly improved Sb_2S_3 sensitized-inorganic-organic heterojunction solar cells and quantification of traps by deep-level transient spectroscopy, *Adv. Funct. Mater.*, 2014, **24**(23), 3587–3592.